



# On numerical energy conservation for an implicit particle-in-cell method coupled with a binary Monte-Carlo algorithm for Coulomb collisions

Justin Ray Angus\*, Anthony Link, Alex Friedman, Debojyoti Ghosh, Jamal David Johnson

Lawrence Livermore National Laboratory, Livermore, CA 94551, USA

## ARTICLE INFO

### Article history:

Received 29 June 2021

Received in revised form 16 November 2021

Accepted 27 January 2022

Available online 2 February 2022

### Keywords:

Plasma

Particle-in-cell

PIC

Boltzmann equation

## ABSTRACT

Conventional particle-in-cell (PIC) methods suffer from enhanced numerical heating (explicit PIC) or cooling (semi-implicit PIC) when coupled with a binary Monte-Carlo algorithm for Coulomb collisions. In this work, a fully-implicit  $\theta$ -PIC scheme (with adjustable time-biasing parameter  $1/2 \leq \theta \leq 1$ ) is considered. The discrete change in energy of a closed system after a time step for this scheme scales with  $(1/2 - \theta)C_\theta$ , where  $C_\theta$  is a positive definite quantity that depends on the frequency spectrum of the energy in the fields. Collisions lead to additional energy in the field fluctuations associated with high-frequency light waves produced by a numerical Bremsstrahlung process, which can result in a large increase in the numerical cooling rate for  $\theta > 1/2$ . However, for  $\theta = 1/2$ , energy is *exactly* conserved. The energy in the field fluctuations on long time scales agrees with that calculated using the equipartition theorem for a classical system in thermodynamic equilibrium.

Published by Elsevier Inc.

## 1. Introduction

The coupled Maxwell-Boltzmann set of equations provides a general kinetic description of ideal plasma systems that includes both long-range (collective) and short-range (collisional) physics. The particle-in-cell (PIC) method is a numerical approach that captures collective plasma effects and is commonly applied to study kinetic physics in weakly-collisional plasmas. In many situations, the effects of collisions, or short-range interactions, are also important. Collisional processes can be modeled effectively using binary Monte-Carlo collision (MCC) algorithms [1]. In a fully-ionized ideal plasma, the important short-range interactions are screened Coulomb collisions as governed by the Landau-Fokker-Planck collision operator. The binary MCC algorithms by Takizuka and Abe [2] and Nanbu [3] are two such algorithms for modeling this process [4].

Coupling a PIC algorithm with a binary MCC algorithm is straightforward in practice and gives a general kinetic description of plasma systems. However, it is often found that the coupling of these two algorithms leads to a rapid unphysical change of the energy in the system. This is true even when the PIC and MCC algorithms independently conserve energy well. Explicit PIC-MCC models are known to rapidly heat the plasma [5], while implicit PIC-MCC models typically display rapid numerical plasma cooling [6]. The work by Angus *et al.* in Ref. [6] used the direct-implicit PIC scheme (which is a

\* Corresponding author.

E-mail address: [angus1@llnl.gov](mailto:angus1@llnl.gov) (J.R. Angus).

semi-implicit scheme) [7] coupled with the binary MCC model by Nanbu [3] as implemented in the multi-physics code Chicago [8] to study the dynamic formation of a Z-pinch in 1D. In that work, many particles per cell are used to minimize the numerical cooling associated with the collisions. Minimizing the numerical cooling is important for that problem as it can lead to unphysically small compression ratios and can have a strong effect on the shock-flash neutron yield formation.

The understanding of why PIC-MCC models suffer from a severe failure to conserve energy has only recently been investigated. To the best of our knowledge, the work by Alves *et al.* in Ref. [5] is the first such work to investigate the numerical root of this problem. The classic leap-frog explicit PIC scheme [9] coupled with the binary MCC algorithm for Coulomb collisions by Takizuka and Abe [2] is used in Ref. [5]. They explored how the numerical heating rate scaled with the physical and numerical parameters of the system by considering a uniform plasma in thermal equilibrium in a periodic box. It is argued in Ref. [5] that the enhanced numerical heating results from the plasma absorbing artificial electromagnetic radiation produced by the stochastic nature of the particles caused by collisions in a numerical Bremsstrahlung-like process. The numerical heating rate is shown to scale with the variance of the current density resulting from the collision model.

Conventional implicit PIC methods, which are semi-implicit, were developed for kinetic studies of low-frequency plasma phenomena without the time step restraints set by explicit algorithms [10,11]. In recent years, new fully-implicit PIC methods have been developed with the attractive property of *exact* energy conservation [12,13]. In this work, we investigate the coupled PIC-MCC model considering a fully-implicit  $\theta$ -PIC scheme where  $1/2 \leq \theta \leq 1$  is an implicit biasing parameter [11]. The *exactly* energy conserving scheme by Markidis and Lapenta [13] is a special case of this method for  $\theta = 1/2$ . The discrete change in energy of a closed system after a time step for this scheme scales directly with  $(1/2 - \theta)C_\theta$ , where  $C_\theta$  is a positive definite quantity (defined later in Eq. (26)) that depends on the frequency spectrum of the energy in the fields. This relation is valid independent of whether collisions are included. In contrast to explicit PIC schemes, which typically heat, the  $\theta$ -PIC scheme always numerically cools for  $\theta > 1/2$ . The inclusion of collisions can significantly change the spectral properties of the field fluctuations in such a way that the numerical cooling rate for  $\theta > 1/2$  is greatly enhanced. However, for  $\theta = 1/2$ , the system neither heats nor cools and energy is *exactly* conserved with or without collisions included.

The remainder of this paper is outlined as follows. In the following section, Sec. 2, the setup for the numerical test problem used to investigate energy conservation for coupled PIC-MCC algorithms is discussed. Results from this problem using an explicit PIC scheme with and without collisions are presented to illustrate the inherent energy conservation problem when conventional PIC methods are coupled with a collision model. The fully-implicit  $\theta$ -PIC algorithm, which is the main focus of this work, is presented in Sec. 3. The discrete numerical energy conservation law for this method in a periodic domain is presented. In Sec. 4, the numerical energy conservation test problem is simulated with the fully-implicit  $\theta$ -PIC model. Important observations from these results are elucidated and discussed. Further discussion on some of the results is given in Sec. 5.

## 2. The numerical energy conservation test for coupled PIC-MCC algorithms

The physical system considered here to investigate numerical energy conservation for coupled PIC-MCC models is chosen to be the same as that considered in Ref. [5], which is a uniform electron-proton plasma in a periodic box. The plasma is initialized at thermal equilibrium;  $n_0 = n_i = n_e = 1.0 \times 10^{30} / \text{m}^3$  and  $T_0 = T_i = T_e = 100$  eV are chosen as the initial default parameters. These conditions are typical of that found in intense laser-solid interactions as well as in inertial confinement fusion (ICF) research. The simulation domain is periodic in each direction and the domain length in each direction is set to  $10\delta_e$ , where  $\delta_e = c/\omega_{pe}$  is the collisionless skin depth with  $\omega_{pe} = \sqrt{n_0 e^2 / m_e \epsilon_0}$  the plasma frequency. For the parameters used here, the skin depth is  $\delta_e = 5.3$  nm and the plasma period is  $1/\omega_{pe} = 1.77 \times 10^{-2}$  fs. Unless stated otherwise, the grid resolution in each direction is set to  $0.25\delta_e$ , the time step is set by  $\omega_{pe} \Delta t = 0.1$ , and the simulations are initialized using 100 equally-weighted macro-particles per cell ( $N_{ppc} = 100$ ) for each species. The collision times are well resolved as  $\nu_{ei} \approx 0.3\omega_{pe}$ .

All simulation results presented in this work are from 2D electromagnetic simulations in a planar geometry and the binary MCC model is that from Ref. [2]. Collisions are included for all species combinations. The simulations are performed using a new particle code framework written in C++/Fortran that uses the Chombo [14] library for data containers with efficient memory and MPI handling. Results from two separate implementations of the PIC algorithm are presented in this paper. In both schemes, the cloud-in-cell (CIC) method is used for depositing the macro-particle currents to the grid and for interpolating the fields from the grid to the particles for the momentum update. The schemes differ in how they are advanced in time. The first is an explicit PIC (e-PIC) algorithm with leap-frog time integration [9] similar to that considered in Ref. [5]. The second PIC algorithm, which is the main focus of this work, is the fully-implicit  $\theta$ -PIC model mentioned previously. This algorithm is explained in detail in Sec. 3.

The energy-conservation problem when conventional PIC schemes are coupled with MCC algorithms is illustrated in Fig. 1. Here, results are presented from simulations of the numerical energy conservation test problem using the e-PIC (left panel), MCC (middle panel), and coupled e-PIC-MCC (right panel) models. The change in energy,  $\Delta W = W(t) - W(t=0)$ , relative to the initial energy in the system,  $W_0 = 3n_0 T_0 V$  with  $V$  the simulation volume, is shown. The total energy is  $W_{tot} = W_e + W_i + W_{EM}$ , where  $W_e$  and  $W_i$  are the kinetic energy in the electrons and ions, respectively, and  $W_{EM}$  is the energy in the fields. For the pure e-PIC simulation, there is an initial small decrease of particle energy ( $W_{parts} = W_e + W_i$ ) that goes into energy associated with the field fluctuations ( $W_{EM}$ ), but the change in total energy is insignificant on this time scale. While there is some small transfer of energy between the electrons and ions for a pure MCC simulation,  $\Delta W_{tot}$  is

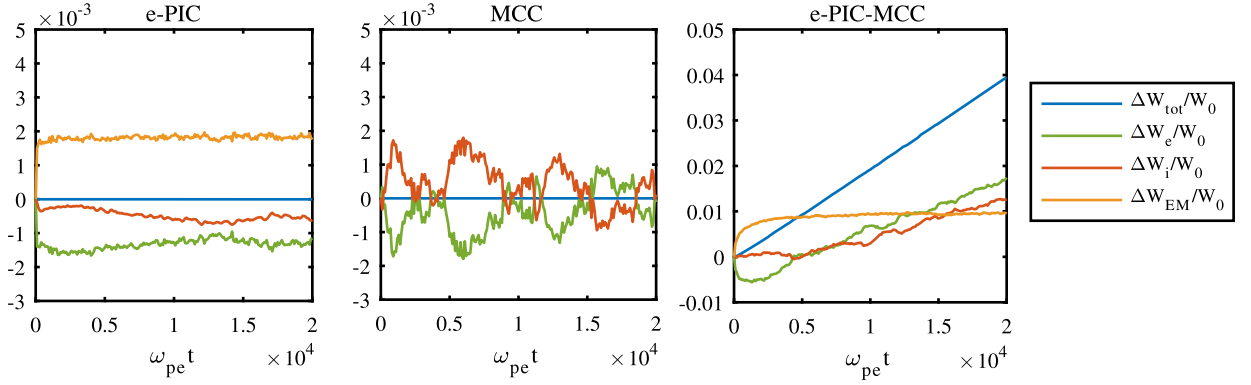


**Fig. 1.** Time history of the relative change of energy from 2D simulations of the numerical energy conservation test problem using a pure e-PIC method (left panel), a pure MCC algorithm (middle panel) and a coupled e-PIC-MCC simulation (right panel). The total energy (blue) is partitioned into electron kinetic energy (green), ion kinetic energy (red), and electromagnetic field energy (yellow). (For interpretation of the colors in the figure(s), the reader is referred to the web version of this article.)

zero to machine precision. Despite the fact that the e-PIC and MCC algorithms both conserve energy well independently, the energy in the plasma is observed to increase linearly with time when these two models are coupled together, as observed in the right panel of Fig. 1.

Results analogous to those shown in Fig. 1 are shown in Fig. 1 of Ref. [5] using their e-PIC model (in 1D). The heating rate observed here is essentially the same as that reported in Ref. [5] for 2D e-PIC-MCC simulations and leads to about a 4% increase of the plasma energy over  $2 \times 10^4$  plasma periods (or  $6 \times 10^3$  electron-ion collision times). It is shown in Ref. [5] that the heating rate for their e-PIC scheme when coupled with a binary MCC algorithm ( $\Gamma_{eMC}$ ) can be related to the variance in the current density fluctuations from the collision model. For a closed electron-ion plasma system in thermal equilibrium, the heating rate scales as

$$\Gamma_{eMC} \propto \frac{\nu_{ei} (\omega_{pe} \Delta t)^2}{N_{ppc}} \xi_0 \frac{T}{T_0}, \quad (1)$$

where  $\nu_{ei} \sim n/T^{3/2}$  is the electron-ion collision frequency and  $\xi_0 = 3n_0 T_0$  is the initial energy density of the system. We have determined that the scaling law for the heating rate given in Eq. (1) also holds for the e-PIC model used in this work. This determination was obtained empirically by looking at how  $\Gamma_{eMC}$  changes when independently varying  $\omega_{pe} \Delta t$ ,  $n_0$ ,  $T_0$ , and  $N_{ppc}$ .

Despite the appearance of the left panel of Fig. 1, energy is not *exactly* conserved in the e-PIC model (see Fig. A.8 in Appendix A). The non-*exact* conservation of energy with the explicit time integration leads to rapid numerical heating when collisions are included. In our experiences, semi-implicit PIC models also experience a rapid, unphysical change of the energy when coupled with a MCC algorithm, but the plasma cools rather than heats. Thus, the numerical effect of collisions is dependent on the PIC scheme being used. The remainder of this paper is dedicated to an investigation of the coupled PIC-MCC model considering a fully-implicit  $\theta$ -PIC scheme.

### 3. The fully-implicit $\theta$ -PIC-MCC algorithm

The implicit  $\theta$ -PIC-MCC algorithm, as implemented and used for the simulations to be presented in this work, is described in this section. Starting with a presentation of the Maxwell-Boltzmann set of equations to be solved, the discrete numerical formulation follows. A discrete energy conservation law for this scheme in a periodic system is presented.

#### 3.1. The Maxwell-Boltzmann set of equations

The Boltzmann equation governing the evolution of the phase-space distribution function  $f_\alpha$  of species  $\alpha$  can be written as

$$\frac{\partial f_\alpha}{\partial t} + \sum_{i=1}^3 \left[ \dot{x}_i \frac{\partial f_\alpha}{\partial x_i} + \dot{v}_i \frac{\partial f_\alpha}{\partial v_i} \right] = C_\alpha, \quad (2)$$

where  $v_i \equiv \dot{x}_i$  and  $C_\alpha$  represents the collision operator of species  $\alpha$  with all species. The time derivatives of the phase space coordinates,  $\dot{x}_i$  and  $\dot{v}_i$ , are obtained from the equations of motion, which in the non-relativistic limit are

$$\frac{d\mathbf{x}}{dt} = \mathbf{v}, \quad \frac{d\mathbf{v}}{dt} = \frac{q_\alpha}{m_\alpha} [\mathbf{E} + \mathbf{v} \times \mathbf{B}], \quad (3)$$

where  $\mathbf{x} = \sum_{i=1}^3 x_i \hat{\mathbf{e}}_i$ ,  $\mathbf{v} = \sum_{i=1}^3 v_i \hat{\mathbf{e}}_i$ , and  $m_\alpha$  and  $q_\alpha$  are the mass and charge, respectively, of species  $\alpha$ . The electric field,  $\mathbf{E}$ , and magnetic field,  $\mathbf{B}$ , are governed by the laws of Ampère and Faraday:

$$\frac{1}{c^2} \frac{\partial \mathbf{E}}{\partial t} = \nabla \times \mathbf{B} - \mu_0 \mathbf{J}, \quad \frac{\partial \mathbf{B}}{\partial t} = -\nabla \times \mathbf{E}, \quad (4)$$

where  $c = 1/\sqrt{\epsilon_0 \mu_0}$  is the speed of light and  $\mathbf{J}$  is the current density obtained from the distribution functions as

$$\mathbf{J} = \sum_{\alpha \in s} q_\alpha \int_{\mathbf{v}} \mathbf{v} f_\alpha d\mathbf{v}^3. \quad (5)$$

Here, the sum is over all species  $s$ ,  $d\mathbf{v}^3 \equiv \prod_{i=1}^3 dv_i$ , and the velocity-space integral for each species is over all of velocity space. For a fully ionized plasma, the collision operator  $C_\alpha$  in Eq. (2) is that corresponding to screened Coulomb collisions and is given by the Landau-Fokker-Planck equation:

$$C_\alpha = - \sum_{\beta \in s} \frac{\partial}{\partial v_j} \frac{q_\alpha^2 q_\beta^2 \log \Lambda}{8\pi \epsilon_0^2 m_\alpha} \int_{\mathbf{v}'} \left[ \frac{\delta_{jk}}{u} - \frac{u_j u_k}{u^3} \right] \left[ \frac{f_\alpha}{m_\beta} \frac{\partial f_\beta(\mathbf{v}')}{\partial v'_k} - \frac{f_\beta(\mathbf{v}')}{m_\alpha} \frac{\partial f_\alpha}{\partial v_k} \right] d\mathbf{v}', \quad (6)$$

where  $u = |\mathbf{v} - \mathbf{v}'|$  is the relative speed,  $\log \Lambda$  is the Coulomb logarithm, and the sum is over all species. For simplicity and direct comparison with Ref. [5],  $\log \Lambda = 3$  is used in this work. The characteristic collision frequency of species  $\alpha$  with species  $\beta$  is defined to be  $\nu_{\alpha\beta} = q_\alpha^2 q_\beta^2 n_\beta \log \Lambda / (8\pi \epsilon_0^2 \mu_{\alpha\beta}^2 \nu_{\alpha\beta}^4) \times \nu_\alpha \sqrt{\mu_{\alpha\beta}/m_\alpha}$  with  $\mu_{\alpha\beta} = m_\alpha m_\beta / (m_\alpha + m_\beta)$ ,  $\nu_\alpha = \sqrt{T_\alpha/m_\alpha}$ , and  $\nu_{\alpha\beta}^2 = \nu_\alpha^2 + \nu_\beta^2$ .

### 3.2. Numerical algorithm

In a PIC scheme, the distribution function is notionally described as a collection of discrete macro-particles in the Klimintovich sense as

$$f_\alpha(\mathbf{x}, \mathbf{v}, t) \approx \sum_{p \in \alpha} w_p \delta(\mathbf{x} - \mathbf{x}_p(t)) \delta(\mathbf{v} - \mathbf{v}_p(t)), \quad (7)$$

where  $w_p = w$  is the macro-particle weight (assumed constant in this work). The total mass and charge associated with particle  $p \in \alpha$  are  $m_p = w m_\alpha$  and  $q_p = w q_\alpha$ , respectively. In practice, the spatial  $\delta$  function in Eq. (7) is replaced by a finite-width spline in an ‘area weighting’ or ‘cloud-in-cell’ representation as described below.

The numerical algorithm considered in this work for the time evolution of the coupled Boltzmann-Maxwell set of equations is an implicit  $\theta$ -PIC method [11] coupled with the binary MCC model for Coulomb collisions by Takizuka and Abe [2]. The electric and magnetic fields used to advance the system from time  $t_n$  to time  $t_{n+1} = t_n + \Delta t$  are computed using quantities at  $t_{n+\theta}$ , which for arbitrary vector  $\mathbf{h}$  can be expressed as

$$\mathbf{h}^{n+\theta} = (1 - \theta) \mathbf{h}^n + \theta \mathbf{h}^{n+1}. \quad (8)$$

This scheme is unstable for an explicit-biased weighting where  $\theta < 1/2$  [11], so the implicit parameter  $\theta$  must be chosen such that  $1/2 \leq \theta \leq 1$ . The discrete version of the equations governing the phase-space trajectory of the macro-particles (Eqs. (3)) are

$$\frac{\mathbf{x}_p^{n+1} - \mathbf{x}_p^n}{\Delta t} = \bar{\mathbf{v}}_p, \quad \frac{\mathbf{v}_p^{n+1} - \mathbf{v}_p^n}{\Delta t} = \frac{q_p}{m_p} (\mathbf{E}_p^{n+\theta} + \bar{\mathbf{v}}_p \times \mathbf{B}_p^{n+\theta}), \quad (9)$$

where  $\mathbf{E}_p^{n+\theta}$  and  $\mathbf{B}_p^{n+\theta}$  are the fields computed at the time-centered macro-particle position  $\bar{\mathbf{x}}_p \equiv \mathbf{x}_p^{n+1/2} = (\mathbf{x}_p^{n+1} + \mathbf{x}_p^n)/2$  by interpolating the fields from the grid at time  $t_{n+\theta}$ . The discrete versions of the laws of Ampère and Faraday (Eq. (4)) used to advance  $\mathbf{E}$  and  $\mathbf{B}$  at grid location  $\mathbf{x}_g$  are given as

$$\frac{\mathbf{E}_g^{n+1} - \mathbf{E}_g^n}{c^2 \Delta t} = \nabla \times \mathbf{B}_g^{n+\theta} |_g - \mu_0 \bar{\mathbf{J}}_g, \quad \frac{\mathbf{B}_g^{n+1} - \mathbf{B}_g^n}{\Delta t} = -\nabla \times \mathbf{E}_g^{n+\theta} |_g, \quad (10)$$

where  $\bar{\mathbf{J}}_g \equiv \mathbf{J}_g^{n+1/2}$  is the time-centered current density at grid location  $\mathbf{x}_g$  defined as

$$\bar{\mathbf{J}}_g = \sum_s \sum_{p \in s} q_p \bar{\mathbf{v}}_p S(\mathbf{x}_g - \bar{\mathbf{x}}_p) / \Delta V. \quad (11)$$

Here,  $\Delta V = \prod_{i=1}^D \Delta x_i$  is the discrete cell volume for a simulation with  $D$  spatial dimensions,  $\bar{\mathbf{x}}_p$  and  $\bar{\mathbf{v}}_p$  are the time-centered position and velocity of macro-particle  $p$ , and  $S$  is the macro-particle shape function used to interpolate the contribution of

the current density associated with macro-particle  $p$  to grid position  $\mathbf{x}_g$ . The same weighting function used in Eq. (11) to deposit the particle currents to the grid is also used to obtain the fields used in the equation of motion in Eq. (9):

$$\mathbf{E}_p^{n+\theta} = \sum_g S(\mathbf{x}_g - \bar{\mathbf{x}}_p) \mathbf{E}_g^{n+\theta}, \quad \mathbf{B}_p^{n+\theta} = \sum_g S(\mathbf{x}_g - \bar{\mathbf{x}}_p) \mathbf{B}_g^{n+\theta}. \quad (12)$$

For all results presented in this work, the cloud-in-cell (CIC) interpolation method is used:

$$S(\mathbf{x}_g - \mathbf{x}_p) = \prod_{i=1}^D \left( 1 - \frac{|x_{g_i} - x_{p,i}|}{\Delta x_i} \right) \text{ for } |x_{g_i} - x_{p,i}| < \Delta x_i. \quad (13)$$

The standard Yee grid [15] is used for the electric and magnetic fields; the electric field is defined along cell edges and the magnetic field is defined on cell faces. The current density used in Eq. (10) is defined on cell edges, as for  $\mathbf{E}$ . The Yee-grid formalism ensures that the physical condition  $\nabla \cdot \mathbf{B} = 0$  is also satisfied discretely. The grid index  $\mathbf{g} = \{g_0, g_1, g_2\}$  used in the notation above represents physically distinct locations depending on which field quantity is being referred to.

For the simulations presented in this work, the implicit advance of Eqs. (9)-(10), referred to as the PIC advance, is achieved using a Picard iteration scheme. The solution from the previous time step is used as the initial guess for the RHS calculation. This is not the most efficient approach, but it is readily implemented, and convergence is often achieved with fewer than 10 iterations when restricting the time step size to that used in an explicit PIC scheme [16]. After the PIC advance is completed, the final part of the advance is applying the binary MCC algorithm to scatter the macro particle velocities. The full time-advance procedure used here is outlined in detail in Algorithm 1.

---

**Algorithm 1** Numerical procedure for advancing the  $\theta$ -PIC-MCC system.

---

1. Begin with an initial guess from the previous solution at time  $t_n$ :  $\mathbf{E}_g^{n+\theta} = \mathbf{E}_g^n$  and  $\mathbf{B}_g^{n+\theta} = \mathbf{B}_g^n$ ,  $\bar{\mathbf{v}}_p = \mathbf{v}_p^n$ .
  2. Advance particle positions to  $t_{n+1/2}$  using the first equation in Eq. (9):  $\bar{\mathbf{x}}_p = \mathbf{x}_p^n + \frac{\Delta t}{2} \bar{\mathbf{v}}_p$ .
  3. Interpolate the time-biased fields from the grid to  $\bar{\mathbf{x}}_p$  using Eq. (12) to obtain  $\mathbf{E}_p^{n+\theta}$  and  $\mathbf{B}_p^{n+\theta}$ .
  4. Advance particle velocities to  $t_{n+1}$  using the fields obtained from step 3 and the second equation in Eq. (9). Compute  $\bar{\mathbf{v}}_p = (\mathbf{v}_p^{n+1} + \mathbf{v}_p^n) / 2$ .
  5. Using  $\bar{\mathbf{x}}_p$  from step 2 and  $\bar{\mathbf{v}}_p$  from step 4, compute the time-centered current density on the grid using Eq. (11).
  6. Compute the curl of  $\mathbf{E}_g^{n+\theta}$  and the curl of  $\mathbf{B}_g^{n+\theta}$  on the grid.
  7. Recompute the fields on the grid at time  $t_{n+\theta}$  using Eq. (10) with  $\bar{\mathbf{J}}_g$  from step 5 and the curl of the fields from step 6:  $\mathbf{E}_g^{n+\theta} = \mathbf{E}_g^n + c^2 \theta \Delta t (\nabla \times \mathbf{B}_g^{n+\theta}|_g - \bar{\mathbf{J}}_g)$  and  $\mathbf{B}_g^{n+\theta} = \mathbf{B}_g^n - \theta \Delta t \nabla \times \mathbf{E}_g^{n+\theta}|_g$ .
  8. Update the iteration count and compute the relative error in the fields with respect to the previous iteration. If the maximum iteration number or tolerance is not met, then repeat steps 2-7.
  9. Compute particle positions and velocities at time  $t_{n+1}$ :  $\mathbf{x}_p^{n+1} = 2\bar{\mathbf{x}}_p - \mathbf{x}_p^n$  and  $\mathbf{v}_p^{n+1} = 2\bar{\mathbf{v}}_p - \mathbf{v}_p^n$ .
  10. Compute field values at time  $t_{n+1}$  using Eq. (8).
  11. If using collisions, then apply the MCC algorithm to the particle velocities.
  12. Time step complete. Go back to step 1 with  $n \rightarrow n + 1$  to do the next time step.
- 

### 3.3. Discrete energy law of the implicit $\theta$ -PIC algorithm

The  $\theta$ -PIC scheme considered here reduces to the energy conserving PIC method by Markidis and Lapenta [13] for  $\theta = 1/2$ . It is shown in Ref. [13] that this scheme is *exactly* energy conserving for  $\theta = 1/2$ . Here, we present a derivation of the generalized discrete energy conservation law considering arbitrary  $\theta$ . Note that the  $\theta$ -PIC scheme considered here is a special case of the implicit-moment scheme presented by Brackbill and Forslund in Ref. [11]. The main difference is that the *exact* time-centered current density is used in Faraday's law, as opposed to the approximation to  $\bar{\mathbf{J}}$  based on the time advance of a subset of fluid moment equations used in Ref. [11].

For the derivation below, we will make use of the following relation between values at  $t_{n+\theta}$  and time-centered values at  $\bar{t} \equiv t_{n+1/2}$ :

$$\mathbf{h}^{n+\theta} = \bar{\mathbf{h}} + \phi (\mathbf{h}^{n+1} - \mathbf{h}^n), \quad (14)$$

where  $\phi = \theta - 1/2$  is the time-centered implicitness parameter. For simplicity, consider a system in a planar geometry that is periodic in each direction with uniform cell volume  $\Delta V$ . The total discrete energy in the fields at time step  $n$  is defined as

$$W_{EM}^n = W_E^n + W_B^n = \frac{\epsilon_0}{2} \sum_g \mathbf{E}_g^n \cdot \mathbf{E}_g^n \Delta V + \frac{1}{2\mu_0} \sum_g \mathbf{B}_g^n \cdot \mathbf{B}_g^n \Delta V. \quad (15)$$

The discrete change of energy in the electromagnetic fields when going from time  $t_n$  to time  $t_{n+1}$  using the fully-implicit  $\theta$ -PIC scheme is

$$\begin{aligned}
 W_{EM}^{n+1} - W_{EM}^n &= \sum_g \left[ \epsilon_0 \bar{\mathbf{E}}_g \cdot \left( \frac{\mathbf{E}_g^{n+1} - \mathbf{E}_g^n}{\Delta t} \right) + \frac{1}{\mu_0} \bar{\mathbf{B}}_g \cdot \left( \frac{\mathbf{B}_g^{n+1} - \mathbf{B}_g^n}{\Delta t} \right) \right] \Delta V \Delta t, \\
 &= \frac{1}{\mu_0} \sum_g [\bar{\mathbf{E}}_g \cdot \nabla \times \mathbf{B}^{n+\theta}|_g - \bar{\mathbf{B}}_g \cdot \nabla \times \mathbf{E}^{n+\theta}|_g] \Delta V \Delta t - \sum_g \bar{\mathbf{J}}_g \cdot \bar{\mathbf{E}}_g \Delta V \Delta t.
 \end{aligned} \tag{16}$$

The first term on the right-hand side of Eq. (16) is the discrete analog of minus the volume integral of the divergence of the Poynting vector. For a periodic domain, this term discretely integrates to zero when  $\mathbf{E}_g$  and  $\mathbf{B}_g$  (which live in different locations on the grid) are evaluated at the same instance in time. For example,

$$\sum_g [\bar{\mathbf{E}}_g \cdot \nabla \times \bar{\mathbf{B}}|_g - \bar{\mathbf{B}}_g \cdot \nabla \times \bar{\mathbf{E}}|_g] \Delta V = 0. \tag{17}$$

Making use of the relation given in Eq. (17) and using Eq. (14), we can write

$$\begin{aligned}
 \sum_g [\bar{\mathbf{E}}_g \cdot \nabla \times \mathbf{B}^{n+\theta}|_g - \bar{\mathbf{B}}_g \cdot \nabla \times \mathbf{E}^{n+\theta}|_g] &= -\phi \sum_g \left[ (\mathbf{E}_g^{n+1} - \mathbf{E}_g^n) \cdot \nabla \times \mathbf{B}^{n+\theta}|_g - (\mathbf{B}_g^{n+1} - \mathbf{B}_g^n) \cdot \nabla \times \mathbf{E}^{n+\theta}|_g \right] \\
 &= -\frac{\phi}{\Delta t} \sum_g \left[ \frac{|\mathbf{E}_g^{n+1} - \mathbf{E}_g^n|^2}{c^2} + |\mathbf{B}_g^{n+1} - \mathbf{B}_g^n|^2 + \mu_0 \bar{\mathbf{J}}_g \cdot (\mathbf{E}_g^{n+1} - \mathbf{E}_g^n) \Delta t \right].
 \end{aligned} \tag{18}$$

Plugging Eq. (18) into Eq. (16) gives

$$W_{EM}^{n+1} - W_{EM}^n = -\sum_g \bar{\mathbf{J}}_g \cdot \mathbf{E}_g^{n+\theta} \Delta V \Delta t - \phi \sum_g \left[ \epsilon_0 |\mathbf{E}_g^{n+1} - \mathbf{E}_g^n|^2 + \frac{1}{\mu_0} |\mathbf{B}_g^{n+1} - \mathbf{B}_g^n|^2 \right] \Delta V. \tag{19}$$

The energy in the particles at time step  $n$  is defined (unambiguously) to be

$$W_{parts}^n = \sum_s \sum_{p \in s} \frac{m_p}{2} |\mathbf{v}_p^n|^2. \tag{20}$$

The change in energy in the particles after a single PIC advance is

$$\begin{aligned}
 W_{parts}^{n+1} - W_{parts}^n &= \sum_s \sum_{p \in s} m_p \bar{\mathbf{v}}_p \cdot (\mathbf{v}_p^{n+1} - \mathbf{v}_p^n) = \sum_s \sum_{p \in s} q_p \bar{\mathbf{v}}_p \cdot (\mathbf{E}_p^{n+\theta} + \bar{\mathbf{v}}_p \times \mathbf{B}_p^{n+\theta}), \\
 &= \sum_s \sum_{p \in s} q_p \bar{\mathbf{v}}_p \cdot \sum_g S(\mathbf{x}_g - \bar{\mathbf{x}}_p) \mathbf{E}_g^{n+\theta} \Delta t = \sum_g \sum_s \sum_{p \in s} q_p S(\mathbf{x}_g - \bar{\mathbf{x}}_p) \bar{\mathbf{v}}_p \cdot \mathbf{E}_g^{n+\theta} \Delta t \\
 &= \sum_g \bar{\mathbf{J}}_g \cdot \mathbf{E}_g^{n+\theta} \Delta V \Delta t.
 \end{aligned} \tag{21}$$

The last step here is made possible because 1) the same shape function  $S$  used to interpolate the particle currents to the grid is also used to compute the electric field for the equation of motion and 2) the current density and electric field acting on the particles are both computed using the time-centered particle positions. The binary collision algorithm is applied at the end of each PIC advance. For equally-weighted particles, the total momentum and energy for each scattering event between two macro-particles is identically conserved. Thus, Eq. (21) is the total discrete change in particle energy after one complete PIC-MCC advance.

The change in total energy in the system,  $W_{tot} = W_{EM} + W_{parts}$ , when going from time step  $n$  to time step  $n + 1$  is obtained by adding Eqs. (19) and (21) together:

$$W_{tot}^{n+1} - W_{tot}^n = -\phi \sum_g \left[ \epsilon_0 |\mathbf{E}_g^{n+1} - \mathbf{E}_g^n|^2 + \frac{1}{\mu_0} |\mathbf{B}_g^{n+1} - \mathbf{B}_g^n|^2 \right] \Delta V. \tag{22}$$

There are two important aspects of Eq. (22) that are worth discussing. First, the term inside the sum is positive definite and so whether the system heats or cools depends solely on  $\phi = \theta - 1/2$ . This means there is always a net heating for explicit-biased schemes with  $\theta < 1/2$ , a net cooling for implicit-biased schemes  $\theta > 1/2$ , and no heating or cooling for  $\theta = 0$  [13]. However, as mentioned previously, the PIC algorithm considered here is not stable for  $\theta < 1/2$ . The second important aspect is that Eq. (22) is independent of whether collisions are included. Thus, the only way collisions can affect the discrete change in energy after a time step (for equally weighted macro-particles) is indirectly through changing the frequency spectrum and/or magnitude of the energy in the field fluctuations.

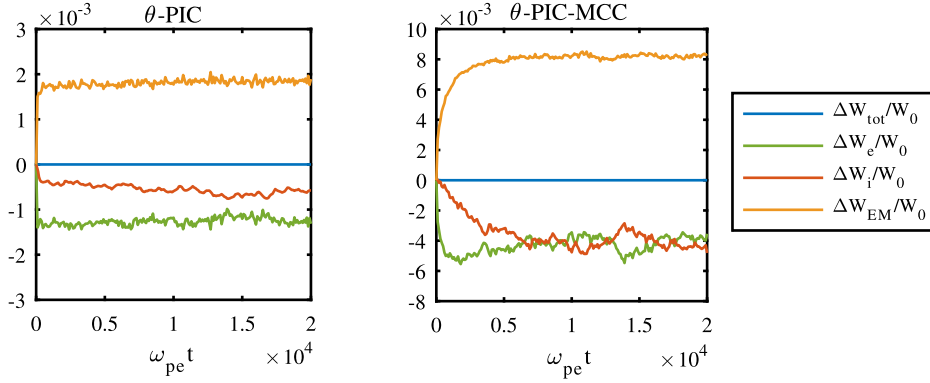


**Fig. 2.** Time history of the relative change of energy from 2D simulations of the numerical energy conservation test problem using the implicit  $\theta$ -PIC scheme with  $\theta = 1/2$ . The total energy (blue) is partitioned into electron kinetic energy (green), ion kinetic energy (red), and electromagnetic field energy (yellow). The results from a  $\theta$ -PIC simulation are shown on the left. The results in the right figure are from a coupled  $\theta$ -PIC-MCC simulation.

#### 4. Numerical energy conservation tests using the fully-implicit $\theta$ -PIC-MCC model

Results are presented in this section from simulations of the numerical energy conservation test problem using the  $\theta$ -PIC and  $\theta$ -PIC-MCC models. The *exactly* energy conserving algorithm with  $\theta = 1/2$  is considered first. Some important observations from these results are discussed. Lastly, the  $\theta$ -PIC algorithm with  $\theta > 1/2$  is examined.

##### 4.1. Results from simulations with $\theta = 1/2$

The same time histories of the relative change in energy shown in Fig. 1 from the e-PIC and e-PIC-MCC simulations are shown in Fig. 2 from  $\theta$ -PIC and  $\theta$ -PIC-MCC simulations using  $\theta = 1/2$ . The picture without collisions for this method is the same as that for the e-PIC method in that there is no significant change in total energy. However, in contrast to the coupled e-PIC-MCC model, total energy is also conserved when the  $\theta$ -PIC algorithm is coupled with the binary MCC model. This is consistent with what is expected from Eq. (22) for  $\theta = 1/2$ .

While the addition of collisions doesn't change the *exact* energy conservation property of the  $\theta$ -PIC scheme with  $\theta = 1/2$ , it is seen in Fig. 2 that the energy associated with the field fluctuations is substantially higher when collisions are included. The enhanced energy in the field fluctuations is associated with the addition of electromagnetic plasma waves produced by a numerical Bremsstrahlung-like process as described in Ref. [5]. The rate of energy gained by the plasma as it absorbs these waves in the e-PIC-MCC model exceeds the rate of energy loss by the plasma in producing the radiation, leading to rapid artificial heating of the plasma. Here, in contrast, after an initial rise of the radiation energy at the expense of energy in the plasma, an equilibrium is achieved where the rate of energy loss by the plasma due to emission is balanced by the rate of absorption.

##### 4.2. Analysis of the energy associated with field fluctuations with and without collisions

The mean component-wise energy in the fields are shown in Fig. 3 from a  $\theta$ -PIC simulation (left panels) and a  $\theta$ -PIC-MCC simulation (middle panels). The difference between the two is shown in the right panels of Fig. 3. The field energy from the collisionless simulation is dominated by in-plane electrostatic fluctuations (Langmuir waves). With collisions, there is a substantial increase in the energy for both the electric and magnetic field. As expected for light waves, the additional energy in each component of the electric field matches the corresponding component of the additional energy in the magnetic field. The energy associated with the out-of-plane component (z-direction) of the light waves is twice that of the in-plane components. This is because the light waves are restricted to in-plane wave vectors ( $k_x$  and  $k_y$ ), in which case there are twice as many sources for the out-of-plane component compared to each of the in-plane components.

Another important observation from Fig. 3 is that the peak amplitude of the mean energy in each component of the electromagnetic radiation for the in-plane components matches that for the electrostatic waves from the collisionless simulations. This result is expected when looking at the system from the point of view of classical statistical mechanics and considering thermal equilibrium. A Hamiltonian can be defined for the total energy in the system as the sum of contributions corresponding to the kinetic energy in the macro-particles,  $H_{kin}$ , and the energy associated with longitudinal electrostatic Langmuir waves,  $H_L$ , and transverse plasma light waves,  $H_T$ . Each of these is defined to be

$$H_{kin} = \sum_s \sum_{p \in s} \frac{1}{2} m_p |\mathbf{v}_p|^2, \quad H_L = \sum_{\mathbf{m}} \frac{\epsilon_0}{2} |\mathbf{E}_{\mathbf{m}}^L|^2 V, \quad H_T = \sum_{\mathbf{m}} \left[ \frac{\epsilon_0}{2} |\mathbf{E}_{\mathbf{m}}^T|^2 + \frac{1}{2\mu_0} |\mathbf{B}_{\mathbf{m}}^T|^2 \right] V, \quad (23)$$

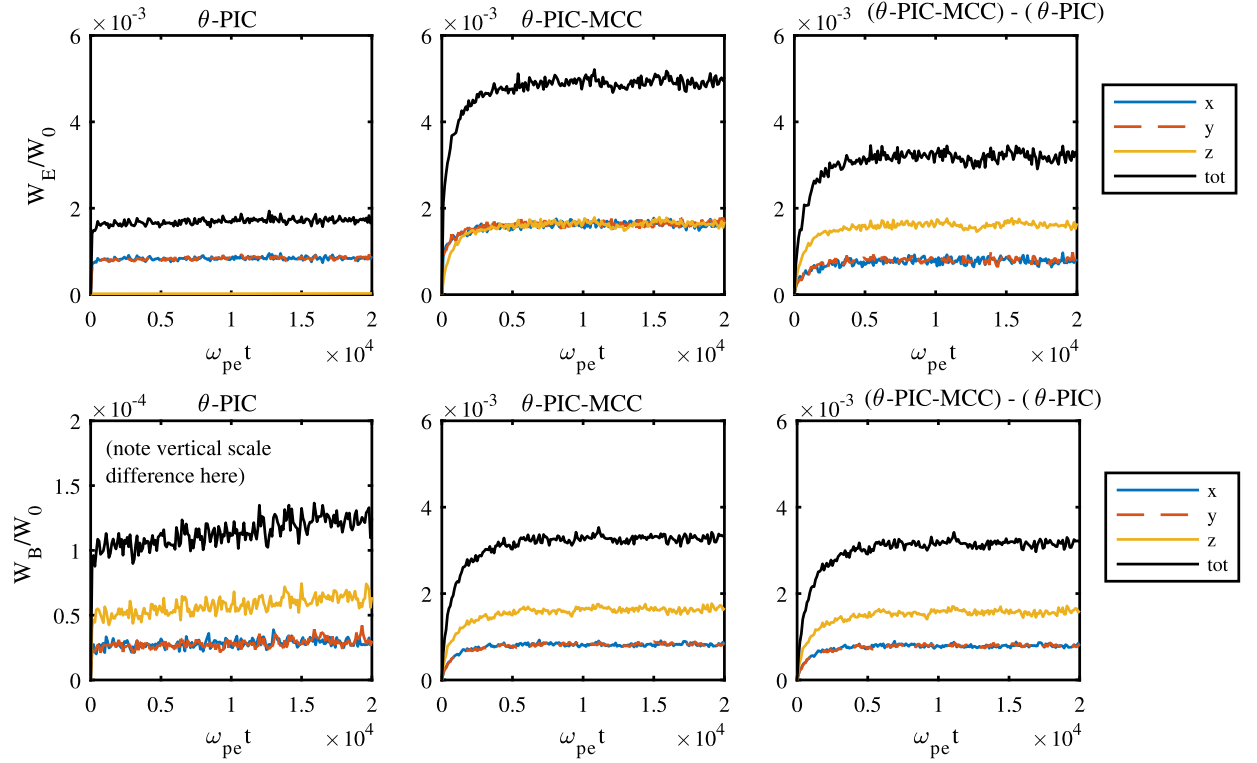


**Fig. 3.** Time history of component-wise energy in the electric field (top row) and magnetic field (bottom row) for a  $\theta$ -PIC simulation (left column) and a  $\theta$ -PIC-MCC simulation (middle column). The difference between the  $\theta$ -PIC-MCC results and the  $\theta$ -PIC results is shown in the right column. Note that the vertical axis for the bottom left panel has a scale that is  $30\times$  smaller than that for the other figures.

where  $\mathbf{m} = \sum_{i=1}^D m_i$  is the vector of discrete mode numbers that correspond to the wavevector  $\mathbf{k} = \sum_{i=1}^D (2\pi m_i/L_i) \hat{\mathbf{e}}_i$  in a periodic domain of length  $L_i$  in spatial direction  $i$  with  $N_i$  grid points. For even  $N_i$ , the discrete mode numbers are  $m_i = -N_i/2:1:N_i/2 - 1$ .  $|\mathbf{E}_m^L|$  is the time-averaged amplitude of the electric field of the electrostatic waves and  $|\mathbf{E}_m^T|$  and  $|\mathbf{B}_m^T|$  are the time-averaged amplitude of the electric and magnetic fields, respectively, of the transverse electromagnetic waves. The expressions for  $H_L$  and  $H_T$  in Eq. (23) are a result of Parseval's theorem for a Fourier series.

The total Hamiltonian of the discrete system is  $H = H_{kin} + H_L + H_T$ . Each component of the sums in Eq. (23) can be viewed as one degree of freedom. Since the Hamiltonian of the discrete system is quadratic with each degree of freedom, the equipartition theorem of classical mechanics states that in thermal equilibrium at temperature  $T$  each of these degrees has an average energy of  $k_B T/2$ . Thus, the ratio of the total energy in the fields to that in the particles in equilibrium is the ratio of the number of degrees of freedom associated with the waves to the number of those associated with the macro-particles. The total degrees of freedom associated with the particles is three times the total number of macro-particles in the simulation. For a system initialized with uniform  $N_{ppc}$  for each species, this gives  $3N_s N_{ppc} N_g$ , where  $N_s$  is the number of species and  $N_g = \pi_{i=1}^D N_i$  is the total number of grid cells. The number of degrees of freedom associated with the electrostatic waves is  $N_g$ . The number of degrees of freedom associated with the electromagnetic waves is four times that for the electrostatic waves. Thus, we can write

$$\frac{H_L}{H} = \frac{N_g}{3N_s N_{ppc} N_g + N_g} = \frac{1}{3N_s N_{ppc} + 1}, \text{ and } \frac{H_L + H_T}{H} = \frac{5N_g}{3N_s N_{ppc} N_g + 5N_g} = \frac{5}{3N_s N_{ppc} + 5}, \quad (24)$$

for the ratio of the field energy to the total energy in the PIC and PIC-MCC models, respectively. For a two species system with  $N_{ppc} = 100$ , this gives  $H_L/H = 1/601 \approx 0.00166$  and  $(H_L + H_T)/H = 5/605 \approx 0.00826$ . These value for  $H_L/H$  and  $(H_L + H_T)/H$  agree well with  $W_{EM}/W_0$  shown in the left and right panels, respectively, of both Fig. 1 and Fig. 2.

It is evident from the above analysis that the peak amplitude of the energy in the field fluctuations is independent of how collisional the plasma is. Via Eq. (24), the energy in the field fluctuations scales with the thermal plasma energy divided by the number of particles per cell. The characteristic collision time scales of the plasma only affect the time scale for the electromagnetic waves to come into thermal equilibrium with the rest of the system. This is all illustrated in Fig. 4 where time histories of the energy in the fields are shown from simulations with varying characteristic collision times. The time-axis is physical time in the left panel and  $v_{ei}t$  in the right panel. The time-histories of the electromagnetic energies from the simulations all match when plotted versus  $v_{ei}t$  for fixed  $N_{ppc}$  and agree with that predicted by Eq. (24) for  $v_{ei}t \gg 1$ .

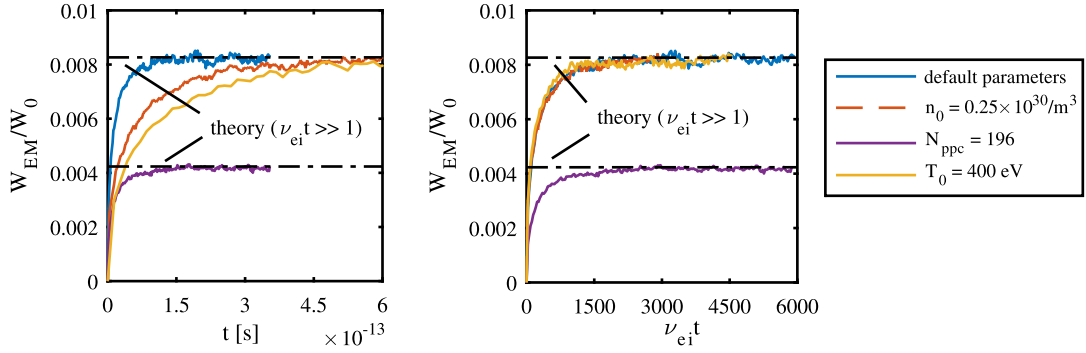


**Fig. 4.** Time history of the relative energy in the field fluctuations from the numerical energy conservation test using the  $\theta$ -PIC-MCC scheme with  $\theta = 1/2$ . The blue curve is obtained using the default simulation parameters as described in the text. The other curves are each obtained for an alternative value of each key parameter as listed in the label. The curves are shown vs time  $t$  in seconds in the left panel and vs  $\nu_{ei}t$  in the right panel. The black dashed-dot lines in the right panel are the expected amplitudes from Eq. (24) for  $\nu_{ei}t \gg 1$ .

#### 4.3. Expected effect of collisions on the numerical cooling rate for $\phi > 0$

One may want to consider a non-zero  $\phi$  to provide some damping of under-resolved waves [17,18]. In order to analyze the numerical cooling for  $\phi > 0$ , Eq. (22) is rewritten as a rate of change law for the spatially averaged total energy density,  $\xi = W_{tot}/V$ , as

$$\Gamma_{\theta} \equiv \frac{\Delta \xi}{\Delta t} = -C_{\theta} \frac{\phi \omega_{pe} \Delta t}{N_{ppc}} \omega_{pe} 3nT, \quad (25)$$

where  $C_{\theta}$  is a dimensionless coefficient defined as

$$C_{\theta} = \langle |\mathbf{c}_{\theta}|^2 \rangle, \quad |\mathbf{c}_{\theta}|^2 = \frac{N_{ppc}}{3nT \omega_{pe}^2} \left( \epsilon_0 \left| \frac{\mathbf{E}^{n+1} - \mathbf{E}^n}{\Delta t} \right|^2 + \frac{1}{\mu_0} \left| \frac{\mathbf{B}^{n+1} - \mathbf{B}^n}{\Delta t} \right|^2 \right). \quad (26)$$

The bracket notation represents the average of a grid quantity:  $\langle h \rangle \equiv \sum_g h_g \Delta V / V$  for some arbitrary grid function  $h$ . The dimensionless coefficient  $C_{\theta}$  is defined such that it is predominantly a function of  $\phi$  for a uniform plasma in the collisionless limit.

Using Parseval's theorem, the integral term in Eq. (26) can be written as a sum over the modulus square of the Fourier coefficients of the fields weighted by the square of the associated frequency;

$$\left\langle \epsilon_0 \left| \frac{\mathbf{E}^{n+1} - \mathbf{E}^n}{\Delta t} \right|^2 + \frac{1}{\mu_0} \left| \frac{\mathbf{B}^{n+1} - \mathbf{B}^n}{\Delta t} \right|^2 \right\rangle \rightarrow \sum_{\mathbf{m}} \left[ \tilde{\omega}_L^2(\mathbf{k}) \epsilon_0 |\mathbf{E}_{\mathbf{m}}^L|^2 + \tilde{\omega}_T^2(\mathbf{k}) \left( \epsilon_0 |\mathbf{E}_{\mathbf{m}}^T|^2 + \frac{1}{\mu_0} |\mathbf{B}_{\mathbf{m}}^T|^2 \right) \right]. \quad (27)$$

Here, the Fourier coefficients of the fields has been decomposed into their longitudinal (L) and transverse (T) parts corresponding to Langmuir waves and plasma light waves, respectively.  $\tilde{\omega}_L$  and  $\tilde{\omega}_T$  are the associated discrete frequencies of these modes. The analytic expressions for the frequencies associated with these waves are

$$\omega_L^2(\mathbf{k}) = \omega_{pe}^2 + 3 \frac{T_e}{m_e} |\mathbf{k}|^2, \quad \omega_T^2(\mathbf{k}) = \omega_{pe}^2 + c^2 |\mathbf{k}|^2. \quad (28)$$

Due to aliasing effects in both space and time, the discrete frequencies present in Eq. (27) will not match well with the analytic expression given in Eq. (28) for under-resolved, high- $k$  modes.

Eqs. (25)-(27) shows that the rate at which the system loses energy for  $\phi > 0$  depends on the discrete frequency spectrum of the energy in the fields. It can be expected that  $C_{\theta}$ , and thus the numerical cooling rate, can be much larger when collisions are included because light waves have a much higher frequency than Langmuir waves for  $v_e = \sqrt{T_e/m_e} \ll c$ . Insights in to how much the cooling rate will be increased by including collisions for small non-zero values of  $\phi$  can be gained by looking at  $C_{\theta}$  from simulations with and without collisions using  $\phi = 0$  (where there is no damping). This is shown in the left panel of Fig. 5 where it is seen that including collisions causes  $C_{\theta}$  to increase by about a factor of 100 on this time scale. Spectral maps of the square modulus of the Fourier coefficients of  $\mathbf{c}_{\theta}$  are also shown from the simulations with and without collisions in Fig. 5. The spectrum is seen to be dominated by the largest wavenumber modes when collisions are included.

$C_{\theta}$  shown in the left panel of Fig. 5 from the simulation with collisions has reached a steady state on the time scale shown, while that from the collisionless simulation is still increasing. Macro-particles in collisionless PIC schemes also have some stochastic component to their orbits, which can lead to the production of electromagnetic radiation. On a much longer

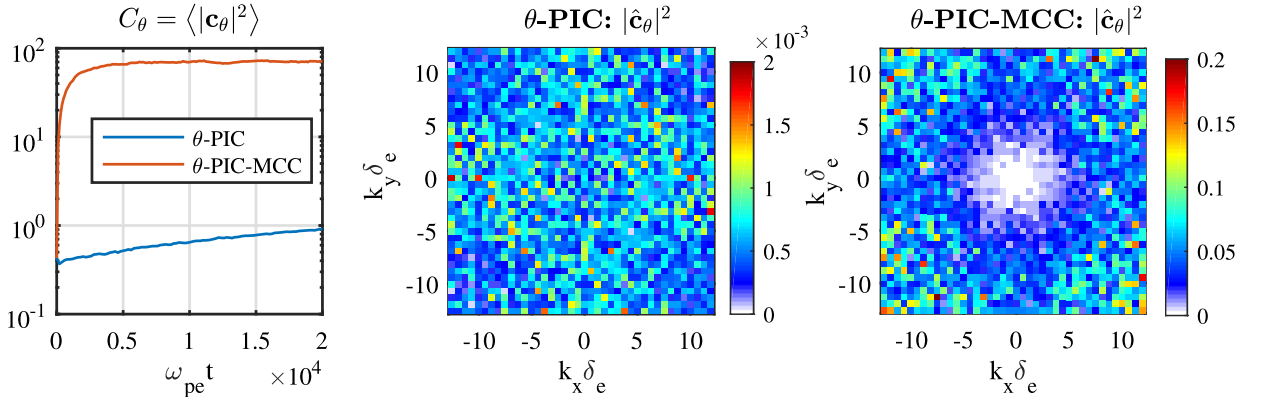


**Fig. 5.** Time history of  $C_\theta = \langle |\mathbf{c}_\theta|^2 \rangle$  (left panel) from simulations with and without collisions using the default parameters and  $\phi = 0$ . The square modulus of the spectral decomposition of  $\mathbf{c}_\theta$  taken at  $\omega_{pe} t = 2 \times 10^4$  from the collisionless and collisional simulations are shown in the middle and right panels respectively. The discrete time derivatives of the fields contained in the definition of  $\mathbf{c}_\theta$  (Eq. (26)) are computed using Eq. (10). Note that the colorbar scale for the figure on the right is 100 times larger than the colorbar scale for the middle figure.

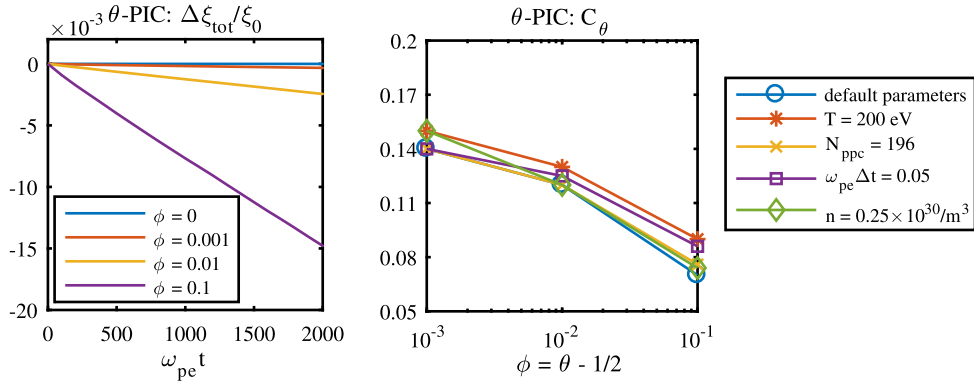


**Fig. 6.** Time history of numerical energy loss using the  $\theta$ -PIC model for different values of  $\phi = \theta - 1/2$  are shown in the left panel. The dimensionless coefficient  $C_\theta$  (Eq. (26)) as a function of  $\phi$  is presented in the right panel. The blue curve is obtained using the default simulation parameters as described in the text. The other curves are each obtained for an alternative value of each key parameters as mentioned in the label. The results obtained at altered density (green) were obtained at fixed values of  $\omega_{pe} \Delta t = 0.1$  and  $\Delta x / \delta_e = \Delta y / \delta_e = 1/4$ .

time scale,  $C_\theta$  from the collisionless simulation will saturate to the same value of  $C_\theta$  from the simulation that includes collisions. This important point is discussed further in Appendix A.

#### 4.4. Results from simulations with $\theta > 1/2$

The effect of a non-zero  $\phi$  on the numerical cooling rate *without* collisions is illustrated in the left panel of Fig. 6. Relatively small deviations from  $\phi = 0$  are considered, ranging from  $\phi = 0.001$  to  $\phi = 0.1$ . The cooling rate roughly increases linearly with  $\phi$  in this range as the coefficient  $C_\theta$  varies weakly going from  $C_\theta \approx 0.15$  at  $\phi = 0.001$  to  $C_\theta \approx 0.8$  at  $\phi = 0.1$ , as illustrated in the right panel of Fig. 6. The weak dependencies of  $C_\theta$  on other parameters, such as time step, particles per cell, temperature, and density, are illustrated in the right panel of Fig. 6.

As discussed previously in Sec. 4.3, the inclusion of collisions can significantly increase  $C_\theta$  through its large effect on the spectral properties of the field fluctuations. This can result in a significantly enhanced cooling rate for  $\phi > 0$  compared to the collisionless case, as shown in Fig. 7. For the default parameters,  $\Gamma_\theta$  is increased by about  $50\times$  for  $\phi = 0.001$  and by about  $4\times$  for  $\phi = 0.1$ . The relatively smaller increase in the cooling rate (with respect to the collisionless case) as  $\phi$  increases is because  $C_\theta$  approximately scales as  $\log \phi / \phi$ , which results in  $\Gamma_\theta \sim \log \phi$ , opposed to the collisionless case where  $\Gamma_\theta \sim \phi$ . Furthermore, how the numerical cooling rate  $\Gamma_\theta$  scales with the remaining physical and numerical parameters is much different than the scalings for the numerical heating rate  $\Gamma_{eMC}$  from the e-PIC-MCC method (Eq. (1)).  $C_\theta$  obtained from simulation with varying values of  $n$ ,  $T$ ,  $\omega_{pe} \Delta t$ , and  $N_{ppc}$  from  $\theta$ -PIC-MCC simulations with non-zero  $\phi$  is shown in the right panel of Fig. 7. For example,  $C_\theta$  actually increases as the time step is reduced, which results in  $\Gamma_\theta \propto (\omega_{pe} \Delta t)^a$  with  $a < 1$ . Recall from Eq. (1) that  $\Gamma_{eMC} \propto (\omega_{pe} \Delta t)^2$ . Moreover, the scaling of  $\Gamma_\theta$  with individual parameters is different for different values of  $\phi$ . There is still a correspondence principle here, in that  $\Gamma_\theta$  reduces as the collision frequency reduces and eventually converges to the collisionless result.

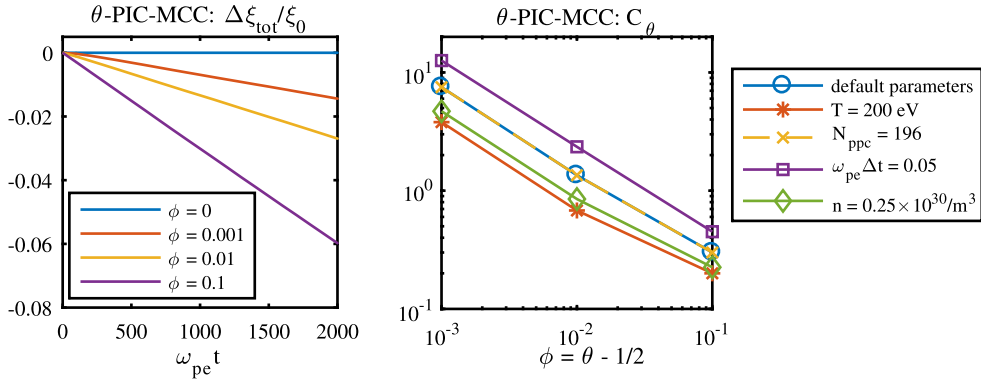


**Fig. 7.** Time history of numerical energy loss using the  $\theta$ -PIC-MCC model for different values of  $\phi = \theta - 1/2$  are shown in the left panel. The dimensionless coefficient  $C_\theta$  (Eq. (26)) as a function of  $\phi$  is presented in the right panel. The remaining details are the same as in Fig. 6. Note the difference in scale here compared to Fig. 6.

## 5. Discussion and conclusions

The numerical energy conservation of a fully-implicit  $\theta$ -PIC scheme when coupled with a binary MCC model for Coulomb collisions is investigated in this work. Simulation of a closed, uniform plasma in thermal equilibrium with and without collisions serves as the testbed for the analysis. The discrete change in total energy after a single PIC advance for this model is derived (Eq. (22)). The change in energy scales directly with  $-\phi C_\theta$ , where  $\phi = \theta - 1/2 \geq 0$  is the time-centered implicit bias parameter and  $C_\theta$  is a dimensionless coefficient that is positive definite and depends on the frequency spectrum of the energy in the fields. The system numerically cools if  $\theta > 1/2$  and conserves energy *exactly* if  $\theta = 1/2$ . This formula also holds when collisions are included if the macro-particles have equal weights. A discussion of some important aspects to consider for the future, such as the effects of macro-particles with unequal weights, large time steps ( $\omega_{pe} \Delta t > 1$ ), and finite plasma systems with physical boundaries, follows.

The macro-particles used in this study have equal weights. In this case, binary MCC algorithms identically conserve total particle energy (and momentum) during each collision step. There are many scenarios where it is more practical to use macro-particles of varying weights. Some examples are high-Z plasmas where the electron density can be much larger than the ion density and/or systems where the plasma density is strongly inhomogeneous. When the macro-particles do not have equal weights, binary MCC models typically only conserve energy on average after many collisions [19,20]. For this scenario, the change in energy in the system after a single PIC-MCC advance would not be identically zero for  $\theta = 1/2$ . However, there would still be no numerical change in energy associated with the PIC advance and thus the full PIC-MCC model should behave the same as the MCC model, in that energy would be conserved on average after many collisions.

The implicit  $\theta$ -PIC scheme as considered here is a fully-implicit method. The discrete energy law presented in Eq. (22) depends on knowledge of the exact future values. Here, a simple iterative scheme is used where the values from the last time step are used as the initial guess. The particles are re-advanced each iteration. Since this is typically the main sink of computational resources in a PIC algorithm, the total computational cost scales almost linearly with the number of iterations. This need for repetition of the particle advance is the main drawback of fully-implicit PIC schemes. However, one advantage of implicit PIC schemes is that the plasma frequency need not be resolved for numerical stability [13]. The extra cost of the fully-implicit solve over an explicit solve can be offset by using a larger time step. How large the time step can be depends on the time scales of the relevant physical processes and will be problem specific. The simple iterative method employed in this work would not be expected to work when under-resolving the plasma frequency. Fully-implicit solutions of the PIC equations using large time steps require use of more advanced methods, such as the *particle-suppressed*, Jacobian-Free Newton-Krylov (JFNK) schemes [21,22,18].

The results presented here are for a uniform plasma in a periodic domain with no physical boundaries. Energy is exactly conserved for the  $\theta$ -PIC scheme for  $\theta = 1/2$  even when coupled to a binary MCC model. However, there is a finite energy density of light waves in the system that is numerical in origin. If the plasma is instead localized in a system with outlet boundaries for radiation, then there would be a finite flux of energy leaving the system. This sink of energy would not register as a direct violation of energy conservation because it would be associated with a Poynting flux, but the Poynting flux itself is numerical in origin. Similarly, this non-physical Poynting flux will result in an artificial transfer of energy from more collisional regions to the less collisional regions in non-uniform plasmas.

As an example, consider a Z-pinch equilibrium where an infinitely long cylindrical plasma column of radius  $a$  with uniform density  $n$  and uniform temperature  $T = T_e = T_i$ . The Z-pinch is confined by a skin current at  $r = a$  and there is no plasma for  $r > a$ . The photon energy density in the simulation can be expressed as  $\xi_{ph} = \alpha \xi_{parts}$ , where  $\xi_{parts} \equiv 3nT$  and, for  $v_{ei} \gg 1$ ,  $\alpha \sim 1/N_{ppc}$  is a constant. The photon energy flux at  $r = a$  leaving the plasma is  $\Gamma_{ph} = \xi_{ph}c$ . The rate of global energy loss of the plasma from this flux is

$$\frac{\Delta(\xi_{parts})}{\Delta t} \pi a^2 = -\Gamma_{ph} 2\pi a, \quad (29)$$

where  $2\pi a$  and  $\pi a^2$  are, respectively, the plasma surface area and volume per unit length. The solution of Eq. (29) is

$$\xi_{parts}(t) = \xi_0 \exp\left(-\frac{2c}{a} \int_0^t \alpha(t') dt'\right), \quad (30)$$

showing that the plasma energy decays exponentially over time. In order to minimize the artificial radiative cooling of the plasma in this scenario, the simulation time would need to be limited such that the exponent in Eq. (30) remains much less than unity. The most straight-forward way to reduce  $\alpha$  is to increase  $N_{ppc}$ , which decreases the ratio of the degrees of freedom in the fields with respect to the total degrees of freedom of the system. However, more particles means more computational effort. Potential methods for increasing the thermal equilibrium time scale of the energy in the light waves, such as altering the collisional dynamics of low-energy particles as discussed in Ref. [5], are a topic for future work.

The results presented in this work are specific to a closed plasma in thermal equilibrium with no physical boundaries. Nevertheless, the *exactly* energy conserving  $\theta$ -PIC scheme ( $\theta = 1/2$ ) does not suffer from the same inherent rapid numerical heating (explicit PIC) or cooling (semi-implicit PIC) that more conventional schemes do when coupled with a binary MCC algorithm. In the future, we plan to implement a *particle-suppressed* JFNK algorithm to efficiently solve the equations when using larger time steps, and to apply the  $\theta$ -PIC-MCC algorithm presented here to physical problems of interest where the combination of collisionless and collisional physics is important.

### Declaration of competing interest

The authors declare that they have no known competing financial interests or personal relationships that could have appeared to influence the work reported in this paper.

### Acknowledgements

This work was performed under the auspices of the U.S. Department of Energy by Lawrence Livermore National Laboratory under Contract DE-AC52-07NA27344 and was supported by the LLNL-LDRD Program under Project No. 21-FS-048.

### Appendix A. Long-time collisionless PIC simulations of a thermal equilibrium plasma

Short-range fields are smoothed out in the PIC method owing to the finite-size of the macro-particles. However, discreteness effects are not completely removed, and the finite-size particles still experience weak, numerically modified collisions [23]. Similar to PIC-MCC models, the stochastic component of the particle orbits leads to the production of electromagnetic radiation. This can be seen from the component-wise energy in the magnetic field in the collisionless case shown in the lower left panel of Fig. 3. For the time scale shown, this energy is an order of magnitude smaller than the energy in the electrostatic modes, but it is slowly growing. The energy associated with field fluctuations in a collisionless PIC simulation for long times (800 times longer than shown previously in Figs. 1-3) is illustrated in Fig. A.8 where it is seen to saturate to a constant value. The results in Fig. A.8 are obtained using the collisionless e-PIC model considering the same default parameters that are used for Figs. 1-3. The inherent numerical heating for the e-PIC model on long times is also illustrated in Fig. A.8.

The steady-state value of  $\Delta W_{EM}/W_0$  is in close agreement with the equipartition value from Eq. (24) ( $\Delta W_{EM}/W_0 = 5/605$ ). However, further partition of the field energy into electric field energy and magnetic field energy shows poorer agreement with the equipartition theorem. The equipartition values are  $\Delta W_E/W_0 = 3/605$  and  $\Delta W_B/W_0 = 2/605$ , but the simulation results show that  $\Delta W_E/W_0$  is slightly less than expected while  $\Delta W_B/W_0$  is slightly larger than expected. To gain some insights into these long-time collisionless PIC simulation results and how they depend on the choice of numerical parameters, a variety of long-time simulations have been ran with different values of  $N_{ppc}$ ,  $\omega_{pe} \Delta t$ , and  $\Delta_x/\delta_e = \Delta_y/\delta_e$ . The main findings are as follows: 1) Changing  $N_{ppc}$  changes the steady state values of  $\Delta W_E/W_0$  and  $\Delta W_B/W_0$  as expected from the equipartition scaling, but does not qualitatively change the results shown in Fig. A.8. 2) Smaller/larger time steps leads to better/worse agreement of  $\Delta W_E/W_0$  and  $\Delta W_B/W_0$  with the equipartition values. 3) The time scale that it takes for energy in the field fluctuations to reach steady state scales inversely with the grid spacing (doubling the spatial resolution doubles the physical time it takes to reach steady state). It may be important to mention that these observations are all from simulations where the Debye length is not resolved. Further analysis of long-time collisionless PIC simulations of thermal equilibrium plasmas could be an interesting topic for future study.

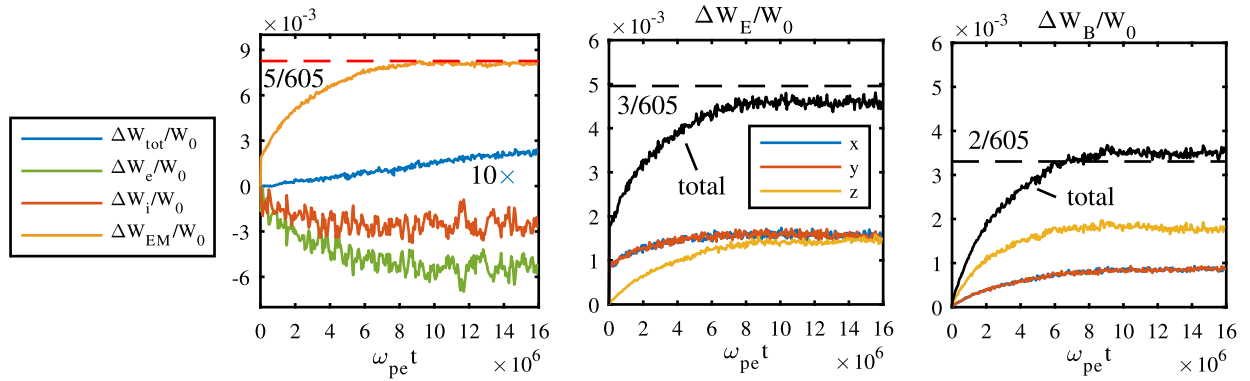


**Fig. A.8.** Time history of the relative change in energy from 2D simulations of the numerical energy conservation test problem using the e-PIC method (no collisions) with the default parameters. The time scale of the simulations is  $800\times$  longer than that shown in Fig. 1. The dashed red line in the left panel is the expected value of  $\Delta W_{EM}/W_0$  for  $t \rightarrow \infty$  from Eq. (24). The  $\Delta W_{tot}/W_0$  curve is magnified by  $10\times$  to show the slow heating inherent in this model. The component-wise relative energy in the electric and magnetic fields is shown in the middle and right panels, respectively. The dashed black curves here are the equipartition values of  $\Delta W_E/W_0$  and  $\Delta W_B/W_0$  for  $t \rightarrow \infty$ .

## References

- [1] K. Nanbu, Probability theory of electron-molecule, ion-molecule, molecule-molecule, and coulomb collisions for particle modeling of materials processing plasmas and cases, *IEEE Trans. Plasma Sci.* 28 (2000) 971–990.
- [2] T. Takizuka, H. Abe, A binary collision model for plasma simulation with a particle code, *J. Comput. Phys.* 25 (1977) 205–219.
- [3] K. Nanbu, Theory of cumulative small-angle collisions in plasmas, *Phys. Rev. E* 55 (1997) 4642–4652.
- [4] C. Wang, T. Lin, R. Caflisch, B.I. Cohen, A.M. Dimits, Particle simulation of coulomb collisions: comparing the methods of takizuka and abe and nanbu, *J. Comput. Phys.* 227 (2008) 4308–4329.
- [5] E.P. Alves, W.B. Mori, F. Fiuza, Numerical heating in particle-in-cell simulations with monte carlo binary collisions, *Phys. Rev. E* 103 (2021) 013306.
- [6] J.R. Angus, A.J. Link, A.E. Schmidt, 1d kinetic study of pinch formation in a dense plasma focus: transition from collisional to collisionless regimes, *Phys. Plasmas* 28 (2021) 010701.
- [7] A. Friedman, A second-order implicit particle mover with adjustable damping, *J. Comput. Phys.* 90 (1990) 292–312.
- [8] C. Thoma, D.R. Welch, R.E. Clark, D.V. Rose, I.E. Golovkin, Hybrid-pic modeling of laser-plasma interactions and hot electron generation in gold hohlraum walls, *Phys. Plasmas* 24 (2017) 062707.
- [9] C.K. Birdsall, A.B. Langdon, *Plasma Physics via Computer Simulation*, McGraw-Hill, New York, 1985.
- [10] B.I. Cohen, A. Langdon, A. Friedman, Implicit time integration for plasma simulation, *J. Comput. Phys.* 46 (1982) 15–38.
- [11] J. Brackbill, D. Forslund, An implicit method for electromagnetic plasma simulation in two dimensions, *J. Comput. Phys.* 46 (1982) 271–308.
- [12] G. Chen, L. Chacón, D. Barnes, An energy- and charge-conserving, implicit, electrostatic particle-in-cell algorithm, *J. Comput. Phys.* 230 (2011) 7018–7036.
- [13] S. Markidis, G. Lapenta, The energy conserving particle-in-cell method, *J. Comput. Phys.* 230 (2011) 7037–7052.
- [14] M. Adams, P. Colella, D.T. Graves, J. Johnson, N. Keen, T.J. Ligocki, D.F. Martin, P. McCorquodale, D. Modiano, P. Schwartz, T. Sternberg, B.V. Straalen, Chombo Software Package for AMR Applications - Design Document, technical report lbnl-6616e ed., Lawrence Berkeley National Laboratory, 2019.
- [15] K. Yee, Numerical solution of initial boundary value problems involving maxwell's equations in isotropic media, *IEEE Trans. Antennas Propag.* 14 (1966) 302–307.
- [16] G. Chen, L. Chacón, L. Yin, B. Albright, D. Stark, R. Bird, A semi-implicit, energy- and charge-conserving particle-in-cell algorithm for the relativistic vlasov-maxwell equations, *J. Comput. Phys.* 407 (2020) 109228.
- [17] G. Lapenta, Exactly energy conserving semi-implicit particle in cell formulation, *J. Comput. Phys.* 334 (2017) 349–366.
- [18] S. Mattei, K. Nishida, M. Onai, J. Lettry, M. Tran, A. Hatayama, A fully-implicit particle-in-cell monte carlo collision code for the simulation of inductively coupled plasmas, *J. Comput. Phys.* 350 (2017) 891–906.
- [19] K. Nanbu, S. Yonemura, Weighted particles in coulomb collision simulations based on the theory of a cumulative scattering angle, *J. Comput. Phys.* 145 (1998) 639–654.
- [20] D.P. Higginson, I. Holod, A. Link, A corrected method for coulomb scattering in arbitrarily weighted particle-in-cell plasma simulations, *J. Comput. Phys.* 413 (2020) 109450.
- [21] W.T. Taitano, Development of a jacobian-free-newton-krylov method with kinetic enslavement to implicitly solve vlasov-poisson system in plasma physics, Ph.D. thesis, University of Idaho, 2010.
- [22] G. Chen, L. Chacón, C. Leibs, D. Knoll, W. Taitano, Fluid preconditioning for newton-krylov-based, fully implicit, electrostatic particle-in-cell simulations, *J. Comput. Phys.* 258 (2014) 555–567.
- [23] J.M. Dawson, Particle simulation of plasmas, *Rev. Mod. Phys.* 55 (1983) 403–447.